

Lithium-Induced Optimization Mechanism for an Ultrathin-Strut Biodegradable Zn-Based Vascular Scaffold

Hongtao Yang, Dawei Jin, Jiancun Rao, Jiahui Shi, Guannan Li, Cheng Wang, Kai Yan, Jing Bai, Guo Bao, Meng Yin,* and Yufeng Zheng*

To reduce incidences of in-stent restenosis and thrombosis, the use of a thinner-strut stent has been clinically proven to be effective. Therefore, the contemporary trend is toward the use of ultrathin-strut ($\leq 70\ \mu\text{m}$) designs for durable stents. However, stents made from biodegradable platforms have failed to achieve intergenerational breakthroughs due to their excessively thick struts. Here, microalloying is used to create an ultrathin-strut ($65\ \mu\text{m}$) zinc (Zn) scaffold with modified biodegradation behavior and improved biofunction, by adding lithium (Li). The scaffold backbone consists of an ultrafine-grained Zn matrix (average grain diameter $2.28\ \mu\text{m}$) with uniformly distributed nanoscale Li-containing phases. Grain refinement and precipitation strengthening enable it to achieve twice the radial strength with only 40% of the strut thickness of the pure Zn scaffold. Adding Li alters the thermodynamic formation pathways of products during scaffold biodegradation, creating an alkaline microenvironment. Li_2CO_3 may actively stabilize this microenvironment due to its higher solubility and better buffering capability than Zn products. The co-release of ionic zinc and lithium enhances the beneficial differential effects on activities of endothelial cells and smooth muscle cells, resulting in good endothelialization and limited intimal hyperplasia in porcine coronary arteries. The findings here may break the predicament of the next-generation biodegradable scaffolds.

Percutaneous coronary intervention using drug-eluting stents (DES) is considered the standard of care to reopen the blocked artery and improve the blood supply of patients. To further improve the efficacy and safety of DES, ultrathin-strut stents are proposed which reduce the strut thickness to less than $70\ \mu\text{m}$. Randomized clinical trials have proven that ultrathin-strut DES is associated with significant reduced risk of in-stent restenosis, and any stent thrombosis compared to the thicker strut DES.^[1] However, the permanent presence of metallic foreign bodies within the artery may cause vascular inflammation, late-stent thrombosis, endothelial dysfunction, and impaired vasomotor function.^[2] Biodegradable scaffolds have been proposed to lead the iteration of DES as they provide temporary scaffolding and then disappear, liberating the treated vessel from its cage and restoring normal functions.^[3] Nevertheless, too-thick strut has become one of the major challenges of biodegradable scaffolds to achieve intergenerational

breakthroughs. The absorb bioresorbable vascular scaffold (Absorb BVS, Abbott Vascular, Santa Clara, CA, USA), composed of biodegradable synthetic polymer (poly-L-lactic acid), was the first U.S. Food and Drug Administration (FDA)-approved fully biodegradable scaffold and received Conformite Europeenne (CE)

1. Introduction

Ischemic heart disease, revealed as the world's number one killer, is responsible for 16% of the world's total death according to the World Health Organization's global health estimates.

H. Yang, J. Shi, G. Li, Y. Zheng
Beijing Advanced Innovation Center for Materials Genome Engineering
& School of Materials Science and Engineering
Peking University
Beijing 100871, P. R. China
E-mail: yfzheng@pku.edu.cn

H. Yang
School of Engineering Medicine
Beihang University
Beijing 100191, P. R. China

D. Jin, M. Yin
Department of Cardiothoracic Surgery
Shanghai Children's Medical Center
School of Medicine
Shanghai Jiao Tong University
1678 Dong Fang Road, Shanghai 200127, P. R. China
E-mail: mengyinmdphd@shsmu.edu.cn


J. Rao
AIM Lab
Maryland NanoCenter
University of Maryland
College Park, MD 20742, USA

C. Wang
Institute of Surface Science
Helmholtz-Zentrum Hereon
21502, Geesthacht, Germany

K. Yan
College of Mechanical Engineering
Yangzhou University
Yangzhou 225127, P. R. China

J. Bai
School of Materials Science and Engineering
Southeast University
Nanjing 211189, P. R. China

G. Bao
Department of Reproduction and Physiology
National Research Institute for Family Planning
Beijing 100081, P. R. China

 The ORCID identification number(s) for the author(s) of this article can be found under <https://doi.org/10.1002/adma.202301074>.

DOI: 10.1002/adma.202301074

mark in 2011.^[4] While, early reports demonstrated the superiority of Absorb BVS, high risk of thrombosis associated with thick struts (150 μm) resulting in a high rate of major adverse cardiac events, which led to the withdrawal of BVS in 2017.^[5] Magmaris (Biotronik AG, Bülach, Switzerland), a magnesium-based biodegradable scaffold (strut thickness 150 μm), though obtained CE approval in 2016, shows further improvements in reducing strut thickness (<100 μm) and extending targeted scaffolding time (>3 months) which are necessary to advance its performance in terms of safety and efficacy.^[6]

Zinc (Zn), exhibiting an intrinsic favorable degradation behavior with satisfying biosafety in vascular environments, has been of particular interest as a promising alternative since 2013.^[7] We initiated the first pure Zn scaffold study and reported that the scaffold maintained mechanical integrity for 6 months and lost 42% scaffold volume after 12 months' implantation in rabbit abdominal aorta.^[8] Nevertheless, the pure Zn scaffold was designed with an unacceptable strut thickness of 165 μm due to its low strength. Zn-alloy scaffolds made of Zn–Cu, Zn–Ag, and Zn–Mg–Cu have been designed to improve the performance of devices. Among them, the Zn–Cu scaffold optimized the structure design, and made an improvement in the mechanical supporting. However, a great gap still exists as the strut thickness of Zn-based scaffolds is larger than 100 μm .^[9] An extraordinary mechanical performance of the material is a prerequisite for the fabrication of vascular scaffolds with ultrathin-strut while providing adequate supporting strength, and undergoing severe plastic deformation without failure. To address this challenge, we systematically investigated a series of alloying elements in terms of mechanical performance, degradation behavior, and biocompatibility.^[10] Our results showed that lithium (Li) was one of the best choices to optimize Zn becoming a qualified scaffold material. Trace amounts of Li (0.1 wt%) enable the Zn alloy to reach an ideal balance between strength and ductility (ultimate tensile strength 431.27 ± 5.89 MPa, elongation $27.96 \pm 6.18\%$) for scaffold application (ultimate tensile strength > 300 MPa; elongation > 20%).^[11] Moreover, Zn–0.1Li alloy also demonstrated a suitable degradation rate (26 ± 5 $\mu\text{m}/\text{year}$) and excellent cytocompatibility for human endothelial cells.

Here, we accomplished the design and fabrication of an ultrathin-strut biodegradable Zn-based scaffold. The fundamental impact of Li in improving the overall performance of biodegradable Zn-based scaffolds has been revealed systematically. The optimizing effects of Li on the microstructure and mechanical properties of the scaffold were studied in terms of grain size distribution, texture, and phase composition. The influence of Li on the biodegradation behavior of the scaffold was revealed from the perspective of interface electrochemical behavior and thermodynamic formation pathways of degradation products. The biological effects of the Zn–0.1Li scaffold are illustrated by evaluating the activities of the major effector cells and corresponding histology in vessel healing.

2. Results

2.1. Microstructure and Performance of the Zn–0.1Li Scaffold

To investigate the impact of Li on the performance of the Zn–0.1Li scaffold systematically, the microstructure of the

Zn–0.1Li alloy microtube is characterized by electron backscatter diffraction (EBSD), X-ray diffraction (XRD), and transmission electron microscopy (TEM), with the pure Zn tube as the control (**Figure 1**). The microtube was fabricated by hot drawing at 200 °C. For the pure Zn tube, dynamic recrystallization resulted in an inhomogeneous coarse microstructure. The average grain diameter was 9.38 μm whereas several large grains (>100 μm) were shown crossing the entire tube wall. The microstructure of the Zn–0.1Li alloy tube exhibited a homogeneous and fine grain size distribution. Around 20% of the grain were refined to sub-micrometer, and the average grain diameter was 2.28 μm . The proportion of the large-angle grain boundary (>15°) in the Zn–0.1Li alloy tube was higher than that of the pure Zn tube. The pole figure showed that the Zn–0.1Li alloy tube maintained a basal plane texture with the basal plane (0001) parallel to the drawing direction. XRD identified the characteristic peaks of the LiZn_4 phase in the Zn matrix. In TEM, the identified LiZn_4 phase was in 100–200 nm. Moreover, precipitates in tens of nanometers (marked by yellow dotted circles) were observed dispersing uniformly in the matrix. The optical morphology of the Zn–0.1Li scaffold during crimp and expansion, and its radial compressive curves are shown in **Figure 1D,E**. The crucial device parameters and performance of representative biodegradable scaffolds compared to durable metallic stents are listed in **Table 1**. The strut thickness of the Zn–0.1Li scaffold was reduced to 65.07 μm , less than 40% of the original pure Zn scaffold, while the radial strength increased from 41.06 to 82.42 kPa. As the thinnest strut in **Table 1**, the radial strength of the Zn–0.1Li scaffold was adequate considering the safety threshold (300 mmHg, 40 kPa) of healthy vessels.^[12] The crossing profile and recoil of the Zn–0.1Li scaffold were superior to the magnesium, polymer, and cobalt–chromium (Co–Cr) scaffolds.

2.2. In Vitro Corrosion Analysis

Figure 2 illustrates the early corrosion features of the Zn–0.1Li alloy in simulated body fluids (SBF). The impedance of Zn–0.1Li alloy is one order of magnitude larger than that of the pure Zn, indicating a better corrosion resistance. Both samples showed a declined trend of impedance over time. The pure Zn exhibited one time constant in the medium to high-frequency zone (10^2 to 10^5 Hz) and stayed unchanged from 1 to 24 h. In Zn–0.1Li alloy, the time constant occupied a wider frequency zone and split into two time constants at 24 h. The time constant is a parameter to describe the relaxation process that happened during the kinetic process of electrode reaction, such as the formation of corrosion products. The time constant at medium to high frequency refers to the charge transfer process of the double-layer capacitance, and the time constant at low frequency may refer to the Li-related inductive reactance. The corrosion morphology was further observed by scanning electron microscopy (SEM). Fine pits were found scattered in the Zn surface while Zn–0.1Li kept almost intact. The chemical composition of corrosion products was examined by X-ray photoelectron spectroscopy (XPS). In pure Zn, the Zn 2p spectrum was fitted into two spin-orbit split peaks at 1021.5 and 1044.4 eV, respectively. The O 1s spectrum had one peak at 530.9 eV which can be assigned to the oxygen of Zn–O, and

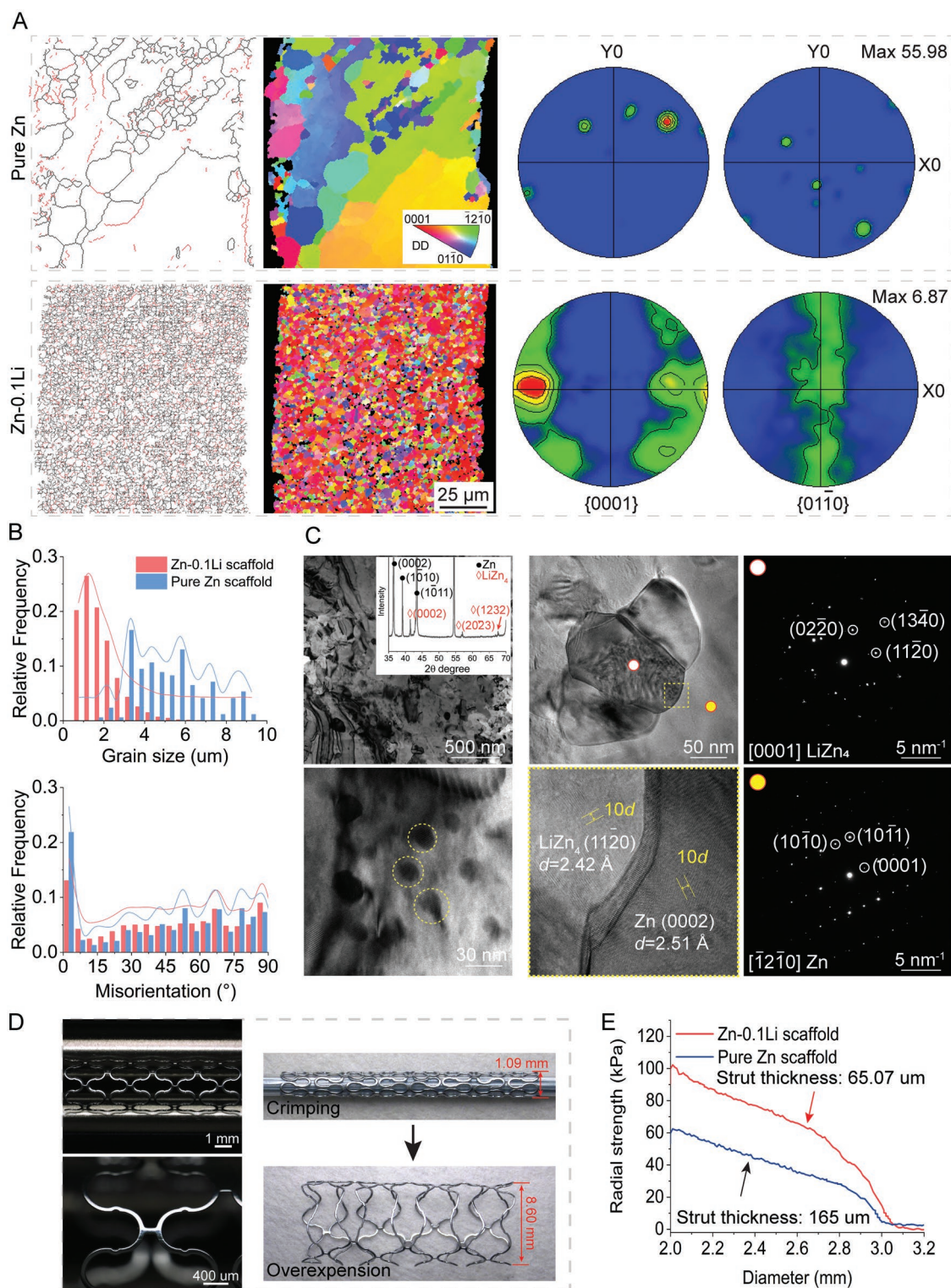


Figure 1. Microstructure and mechanical property of the Zn-0.1Li alloy microtube and scaffold compared with the pure Zn ones. A) Grain boundary maps and EBSD inverse pole figure (IPF) orientation maps of pure Zn and Zn-0.1Li microtubes. Grains with orientations larger and lower than 15° are outlined in black and red, respectively. X0-Y0 plane is perpendicular to the hot drawing direction. B) Quantitative analysis of grain diameter distribution and grain misorientation. C) Bright-field and high-resolution TEM images of the Zn-0.1Li microtube. The white dot and yellow dot indicate the area for the selected-area electron diffraction (SAED) patterns. The yellow dotted square indicates the high-resolution image of the interface between LiZn₄ grain and Zn grain. The XRD pattern of the Zn-0.1Li microtube is inserted in the bright-field image. Nanoprecipitates are marked by yellow dotted circles. D) Optical images of the Zn-0.1Li scaffold after laser cutting, polishing, crimping, and expansion. E) Radial force curves of the Zn-0.1Li scaffold and pure Zn scaffold.

Table 1. Device parameters and performance of representative biodegradable scaffolds and durable metallic stent.

Φ3.0 mm	Strut thickness [μm]	Crossing profile [mm]	Recoil [%]	Foreshortening [%]	Radial strength [kPa]
Pure Zn scaffold ^[8]	165	—	—	—	41.06
Zn–0.8Cu scaffold ^[13]	100	0.8–1	0.41	—	112.6
Zn–0.1Li scaffold	65.07	1.09	0.47	–4.07	82.42
Pure iron scaffold ^[14]	70	1.00	2.24	–1.01	92
Nitrided iron scaffold ^[14]	70	0.99	2.21	–1.22	171
Magmaris ^[15]	150	1.44	4.94	–3.29	—
Absorb GT ^[15]	150	1.38	5.22	–6.91	120 ^[16]
Xience Prime ^[14]	81	1.13	3.6	–2.4	120

another at 531.9 eV related to the oxygen of hydroxyl anion. In Zn–0.1Li alloy, Li₂CO₃ was detected based on the peaks at 55.1 eV (Li 1s), 289.1 eV (C 1s), and 532.1 eV (O 1s) in addition to the products of Zn.^[17] The scanning vibrating electrode technique (SVET) found out that the cathode and anode formed spontaneously within 24 h in the pure Zn sample, which facilitated the formation of pits. In contrast, the surface potential of Zn–0.1Li alloy stayed uniform and stable in the same time period.

2.3. Cellular Evaluations

Endothelial cells and smooth muscle cells are two major effector cells during vessel healing. The impact of scaffold materials on adhesion, proliferation, and migration of human umbilical vein endothelial cells (HUVECs) and human aorta smooth muscle cells (HSMCs) are presented in **Figure 3**. HUVECs were seeded and adhered normally on the surface of pure Zn and Zn–0.1Li alloy. Cells on the Zn–0.1Li alloy exhibited a more spreading morphology with more stretched cytoskeleton after 6 h of seeding compared to the pure Zn sample. The proliferation of HUVECs on sample surfaces is studied by Live/Dead staining. HUVECs proliferated continuously on pure Zn and Zn–Li samples, though their proliferation rates to reach a full confluency were slower than that of 316L SS. However, HSMCs were unable to survive on the pure Zn and Zn–Li samples.

The effect of material extract on cell proliferation is conducted considering the impact of degradation products on cells adjacent to the scaffold materials. The extract of Zn–0.1Li alloy group promoted the proliferation of HUVECs significantly compared to the 316L SS and Zn groups. This promotion effect lasted even after twofold dilution. Undiluted Zn–0.1Li alloy and Zn extracts showed a toxic effect on the HSMCs while one- to three-fold dilution manifested effective inhibition on the proliferation of HSMCs compared to the 316L SS group.

The effect of material on cell migration is further evaluated with extracts at non-cytotoxic concentrations. Both Zn–0.1Li alloy and Zn groups inhibited the migration of HSMCs significantly compared to the control and 316L SS groups. Zn–0.1Li alloy group showed the most inhibition at threefold dilution. For HUVECs, Zn and Zn–0.1Li groups suppressed their migration compared to the 316L SS group. Zn–0.1Li alloy group exhibited significantly less suppression on cell migration

compared to the Zn group, and this effect diminished with dilution.

2.4. Degradation Behavior and Products of the Zn–0.1Li Scaffold in Porcine Coronary Artery

Figure 4 presents the evolution of the degradation behavior of the Zn–0.1Li scaffold with time in porcine coronary at hierarchical levels. Micro-CT images were used here to show the macroscopic behavior, while SEM cross-sectional images provided more detailed information at a microscale (**Figure 4A**). At 1 month, the integrity of the scaffold was maintained, and the crown structure was seen clearly, indicating an excellent radiopacity of the scaffold material. The cross-sectional contour of the strut was intact and clear, showing that uniform corrosion dominated the degradation. Only trace amounts of degradation products were found on the scaffold–tissue interface. At 6 months, deformation and fractures were observed along the scaffold (yellow triangles), implying the loss of mechanical integrity. Significant degradation was found in some struts, but the majority of the metallic matrix remained. At 12 months, further degradation of the scaffold was observed as attenuated struts with flocculent degradation products were prevalent (white triangles). Localized corrosion became the main degradation mode at this stage. Although degradation was seen in most struts, the degree varied greatly. For example, the rectangle profile remained in most struts while one strut (yellow arrow) disintegrated completely. Additionally, degradation products were generated around the strut (yellow asterisks). Quantitative analysis of the degradation results is measured and calculated in **Figure 4B**. The average penetration rates of Zn–0.1Li scaffold at 1, 6, and 12 months were 7.88, 3.92, and 2.93 μm/year, respectively, showing a decreasing trend over time. The cross-sectional area (CSA) reduction and area ratio of degradation products (ARDP) verified the continuous degradation of the scaffold *in vivo*. Also, the data dispersion increased greatly with time, corroborating the transition from uniform corrosion to localized corrosion.

To investigate degradation products of the Zn–0.1Li scaffold during vascular healing, both qualitative and quantitative analysis are performed via energy-dispersive X-ray spectroscopy (EDS) in **Figure 4C**. At 1 month, the scaffold–tissue interface was smooth and intact. A layer of degradation products, which at a thickness of less than 1 μm, was visible covering the metallic matrix. These products were mainly composed of oxygen and

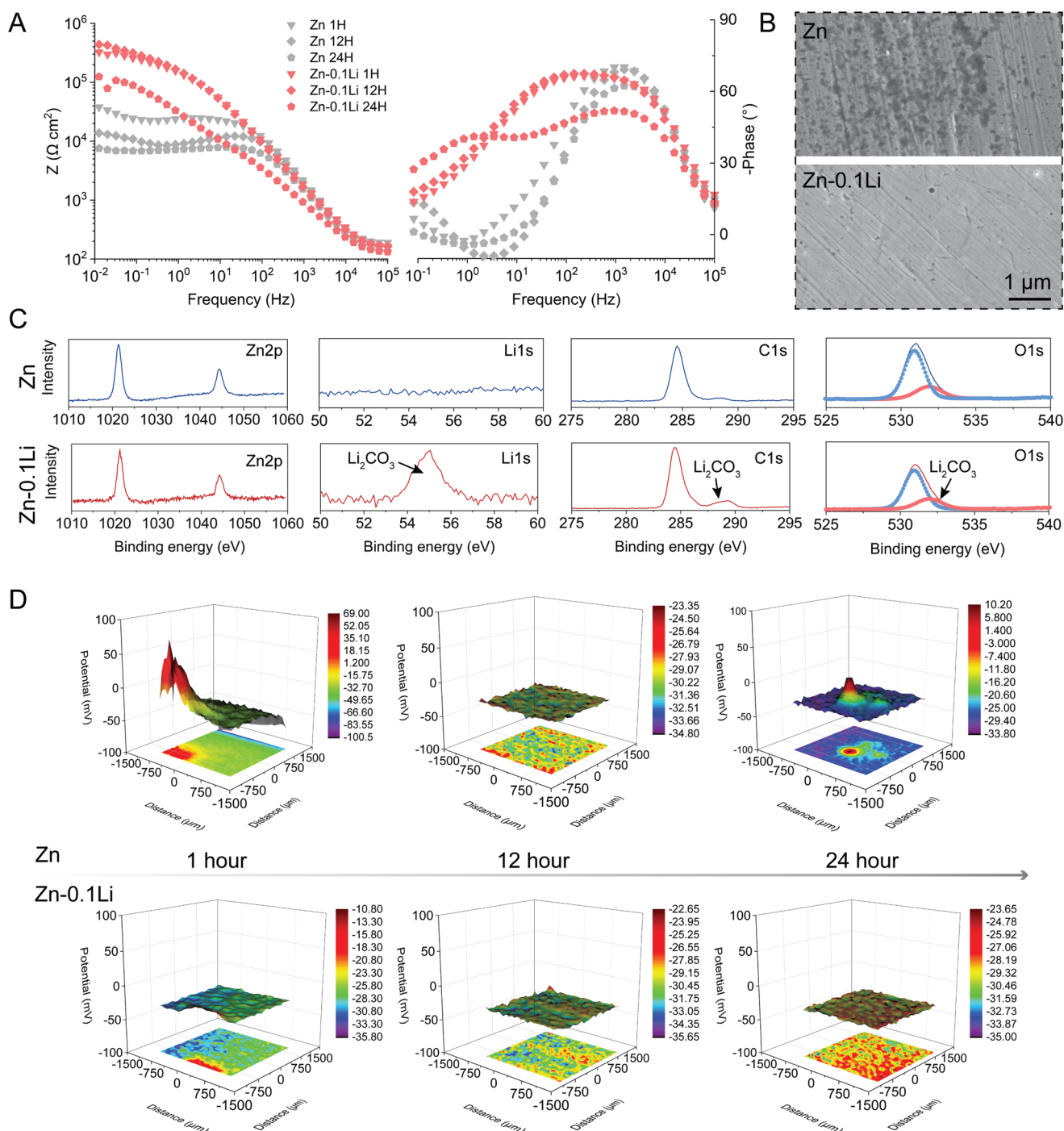


Figure 2. Impact of Li on the corrosion behaviors of Zn in SBF solutions. A) Nyquist plots and Bode plots at 1, 12, and 24 h. B) Corrosion morphology after 24 h-immersion. C) XPS of Zn 2p, Li 1s, C 1s, and O 1s spectra for corrosion products of Zn and Zn-0.1Li alloy after immersion. D) SVET monitoring of potential distribution on sample surface at 1, 12, and 24 h.

zinc, which at a ratio around 1:1, and small amounts of carbon and phosphorus. At 6 and 12 months, the corrosion mode and chemical composition of degradation products changed greatly. Meanwhile, the interface displayed a zigzag feature. The corrosion of the scaffold transformed from a uniform mode to a more localized one. Degradation products diffused toward the

surrounding tissue while penetrating the metallic matrix as well. The chemical composition of products can be roughly divided into three categories. Region 1 (R1), which was located inside the original contour of the scaffold strut, consisted of carbon, oxygen, and zinc. Region 2 (R2), distributed in tissue, had a similar chemical composition to that of the degradation

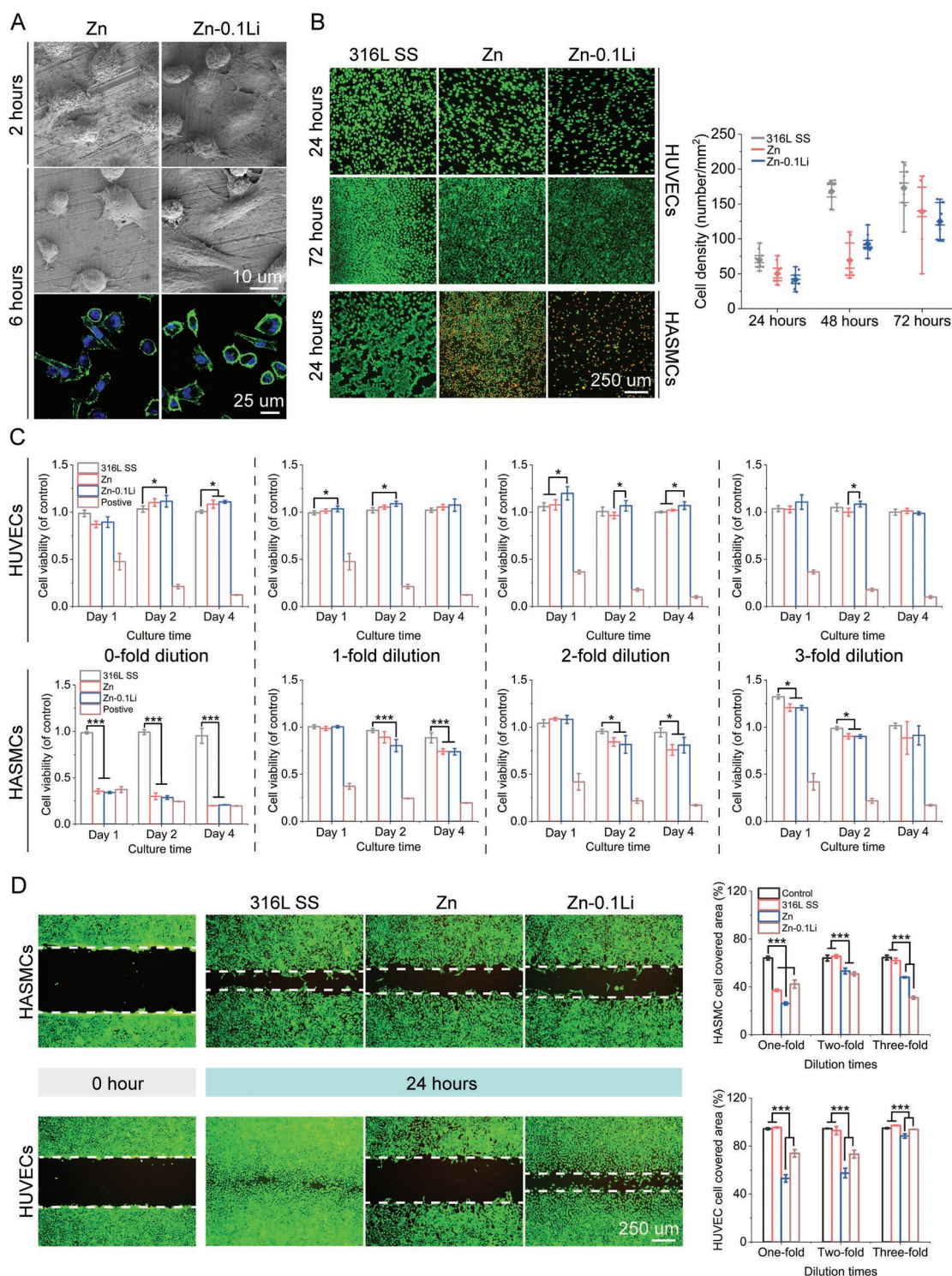


Figure 3. Impact of materials on adhesion, proliferation, and migration of vessel cells. A) Human umbilical vein endothelial cells (HUVECs) morphology after 2 and 6 h adhesion on the surface of Zn and Zn-0.1Li alloy. For fluorescence staining, cell nuclei and actin are stained by DAPI (blue) and FITC (green). B) Live/Dead staining of HUVECs and human aorta smooth muscle cells (HASMCs) at 24 and 72 h proliferation on sample surfaces with corresponding HUVECs number counts ($n = 9$). For box-whiskers plots, the first and third lines correspond to 25th and 75th percentiles, the second line corresponds to median, diamond indicates mean value, and whiskers include minimum and maximum of all data points. C) Cell viability, and proliferation after culturing with zero- to three-fold diluted material extracts ($n = 5$). Ionic concentrations in extracts are listed in Table S1, Supporting Information. D) Cell migration after 24 h-culturing with one- to three-fold diluted material extracts ($n = 3$). Images of Live/Dead staining shows the result of cells cultured with onefold dilution and twofold dilution for HUVECs and HASMCs, respectively. $*p < 0.05$, $**p < 0.01$, $***p < 0.005$.

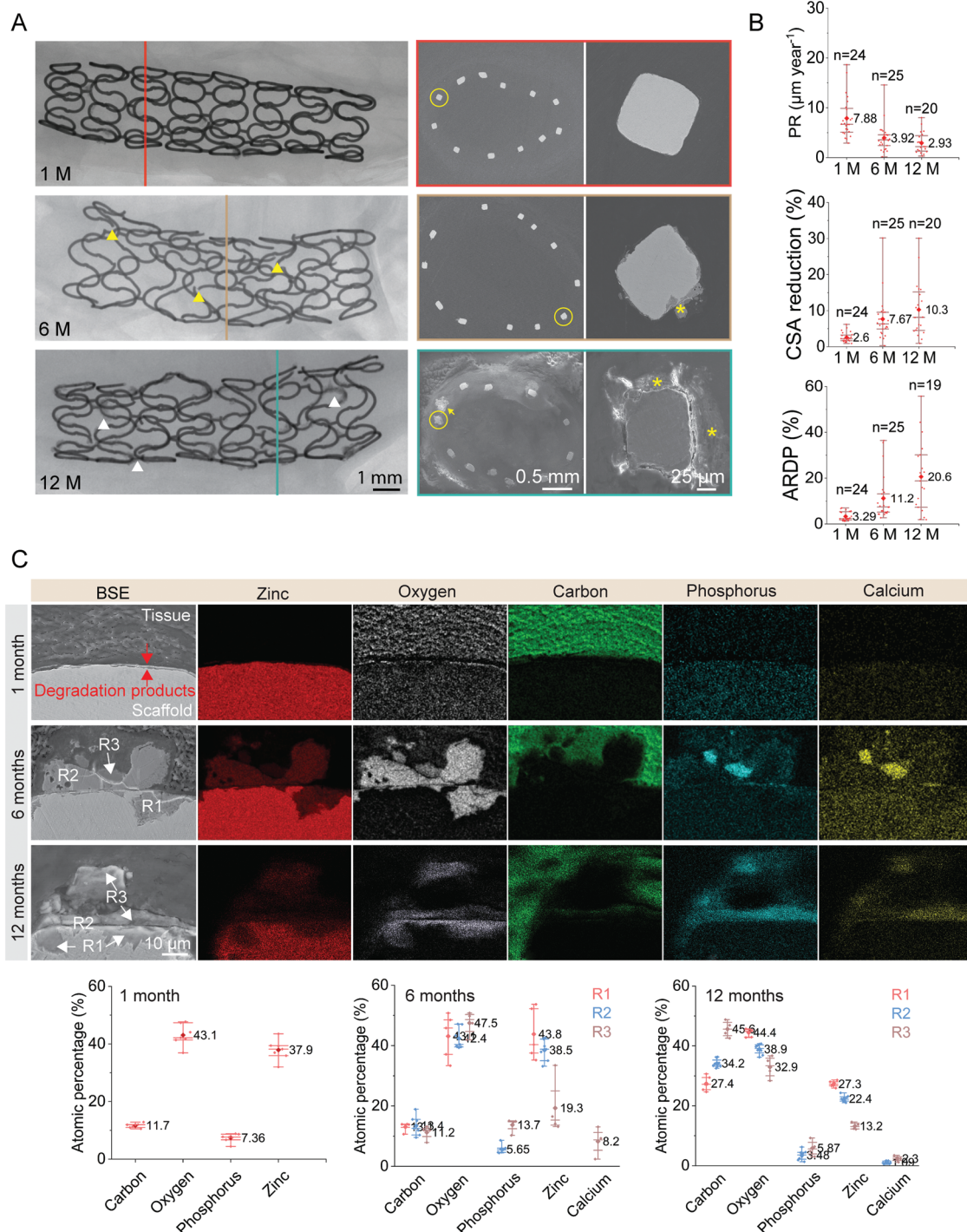


Figure 4. Degradation behavior of the Zn–0.1Li scaffolds in porcine coronary arteries at 1, 6, and 12 months post-surgery. A) Micro-CT images and cross-sectional morphology (SEM images) of Zn–0.1Li scaffolds. Yellow circles: magnifications; yellow triangles: fractures; white triangles: localized corrosion; yellow arrow: disintegrated strut; yellow asterisks: degradation products. B) Quantitative analysis of degradation parameters includes penetration rates (PR), cross-sectional area (CSA) reduction, and area ratio of degradation products (ARDP). 1 month (M), $n = 24$; 6 M, $n = 25$; 12 M, $n = 20$. For the box-whiskers plots, the first and third lines correspond to 25th and 75th percentiles, the second line corresponds to the median, diamonds indicate mean values, and whiskers include minimum and maximum of all data points. C) Elemental mapping on the material–tissue interface with quantitative analysis on regions of interest (R1, R2, R3) at 1, 6, and 12 months ($n = 7$). For the box-whiskers plots, the first and third lines correspond to 25th and 75th percentiles, the second line corresponds to the median, the diamonds indicate the mean value, and the whiskers include minimum and maximum of all data points.

product at 1 month. More phosphorus and calcium while less zinc was detected in region 3 (R3) compared to R1 and R2.

2.5. Identification of Degradation Products

Although EDS provided useful information about the elemental composition of degradation products, it failed to detect Li, which may have a critical impact on the degradation behavior of the Zn–0.1Li scaffold. Time-of-flight secondary-ion mass spectrometry (TOF-SIMS) was performed here to track the trace of Li during degradation. A representative region covering metallic scaffold, degradation products, and tissue was chosen for TOF-SIMS analysis from a 12-month sample (Figure 5). The surface layer of the selected region was removed to avoid signal interference from contaminants before data collection. The TOF-SIMS mapping demonstrates that degradation

products were rich in Li^+ and O^- , with a much weaker signal of C^- and trace amounts of Zn^+ , P^{5+} , and Ca^+ . The SIMS spectrum shows the negative and positive polarity measurements on the selected region. Cations including Li^+ , Zn^+ , and Ca^+ and anions including C^- , O^- , OH^- , and PO_3^{3-} were detected in the mass spectra, respectively. The intensity of peaks is proportional to the number of ions of corresponding elements that are sputtered from the sample. Larger amounts of Li^+ were collected compared to other cations.

A TEM was adopted to gain a deeper understanding of the chemical composition and crystallographic information of degradation products. As shown in Figure S1, Supporting Information, a sample slice ($40 \times 3 \mu\text{m}$) was taken from the region of interest in a severely corroded strut at 12 months by focused ion beam (FIB). The sample slice was sputtered with a layer of tungsten to maintain its integrity. The slice was further thinning for TEM observation. Figure 6 shows the overview of

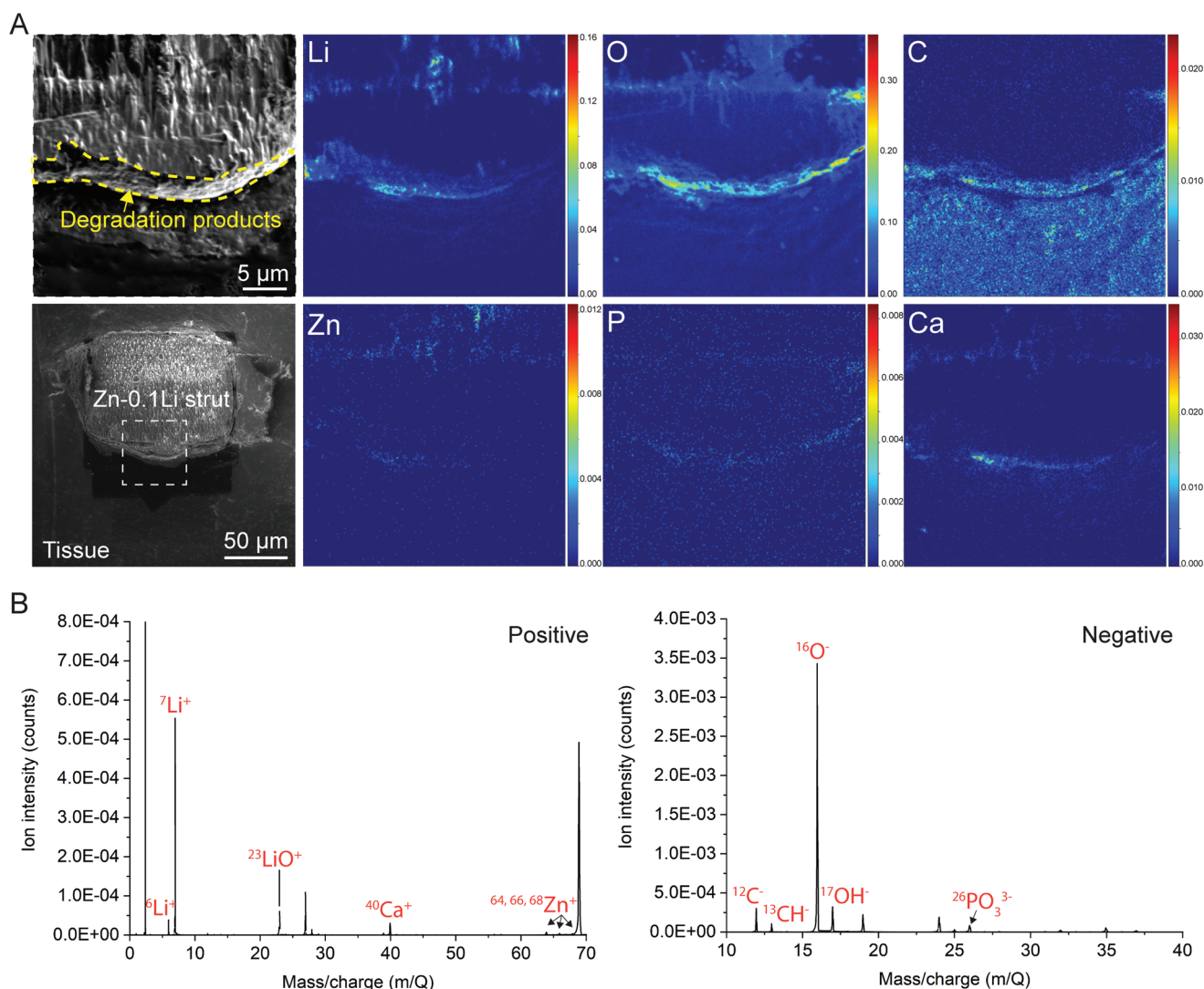


Figure 5. Time-of-flight secondary-ion mass spectrometry (TOF-SIMS) analysis. A) Elemental mapping; the white rectangle indicates the mapping regions. B) TOF-SIMS spectrum of the related ions.

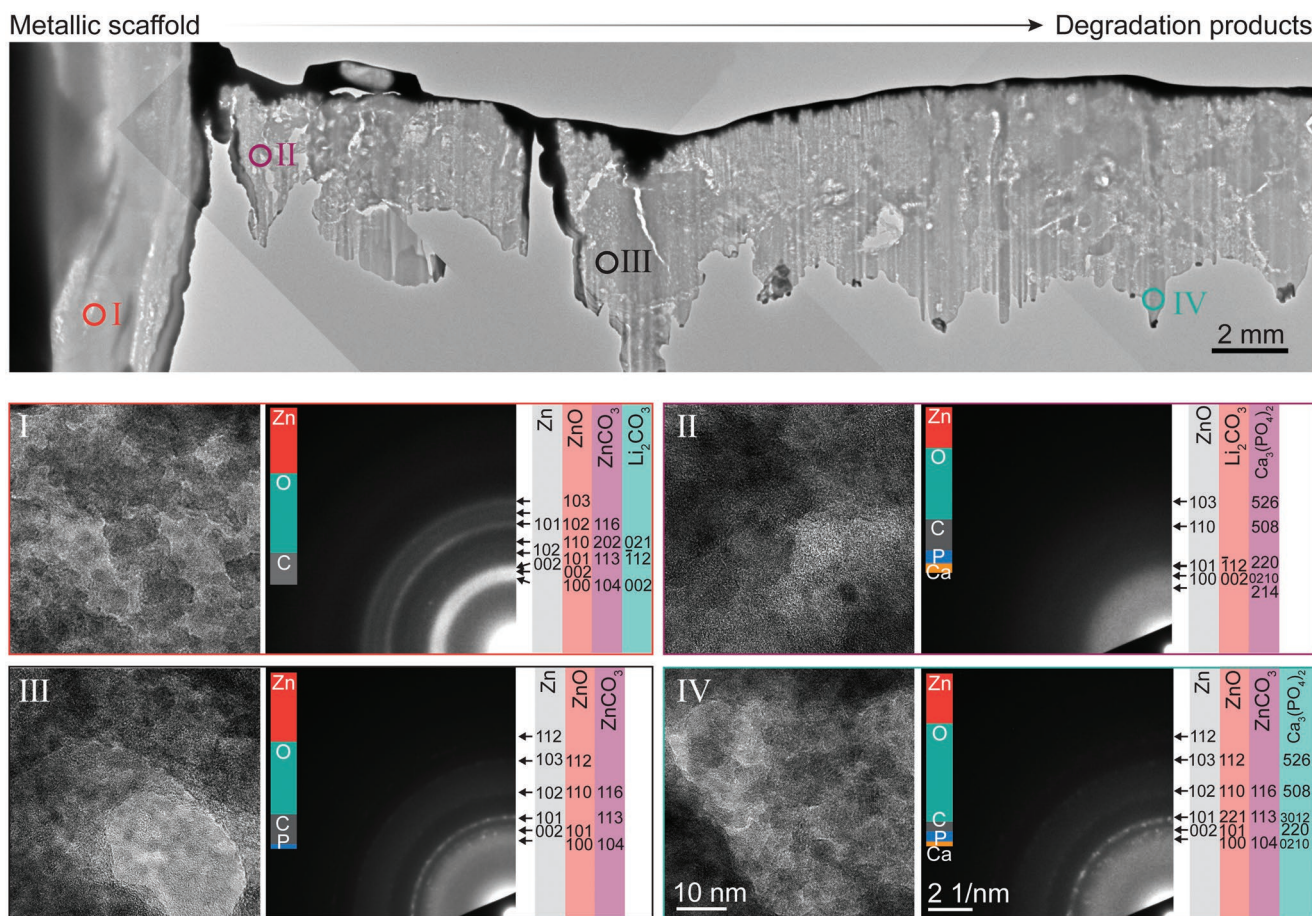


Figure 6. Transmission electron microscopy (TEM) analysis on a representative degraded scaffold strut slice at 12 months. Four regions with numbers I–IV are selected for bright-field images, high-resolution images, and selected area electron diffraction (SAED). The inserted column in the SAED pattern indicates the chemical composition detected in corresponding regions. Identified degradation products with corresponding Miller indices are marked on the right.

the sample slice with bright field images. Detailed information was collected via high-resolution images and selected-area electron diffraction (SAED) in regions I to IV. Region I was a polycrystalline structure with grain size around 5 nm. Zinc, oxygen, and carbon were the major elements in this region. SAED identified products including Zn, ZnO, ZnCO₃, and Li₂CO₃ in this region. For region II, more elements including carbon, phosphorus, and calcium were detected here compared to region I. It consisted an amorphous structure with small grains (2–3 nm) dispersing in it. Here, Ca₃(PO₄)₂ was found in addition to ZnO and Li₂CO₃. Region III and IV presented a similar polycrystalline structure to region I. They were both composed of Zn, ZnO, and ZnCO₃ while Ca₃(PO₄)₂ was also found in Region IV.

2.6. Optical Coherence Tomography and Histological Assessments

To study the deployment of the scaffold after implantation and assess the healing progress of the artery over time, optical coherence tomography (OCT) was adopted and results are

shown in Figure 7. At 1 month, individual scaffold struts were recognized as highly reflective structures (yellow arrows) with dorsal shadow against the vessel wall, indicating a good strut apposition. Also, a thin neointimal layer was found covering the struts, revealing a healthy endothelialization process. A three-layered structure of intima, media, and adventitia (white arrows) was discernible by OCT. At 6 and 12 months, the attenuation of signal around the edge of struts remained sharp, implying that scaffold struts were still composed of considerable amounts of metallic matrix. Importantly, OCT demonstrated an optically homogeneous vessel wall structure with a smooth appearance of the endoluminal lining, suggesting a favorable healing process of the artery. No malapposition or thrombus was found during the implantation. A positive remodeling of the artery was suggested as the lumen area increased while the scaffold area became steady over time (Figure 8B–D). Also, the neointimal area underwent an increase from 1 to 6 months followed by a decline at 12 months. The lumen diameter stenosis at 12 months (20.08 ± 3.1%) is well below the diagnostic threshold for stenosis (50%). Pathological evaluations are performed by hematoxylin–eosin (H&E) and Masson staining (Figure 7E). The 65 μm strut thickness of the Zn–0.1Li scaffold facilitated

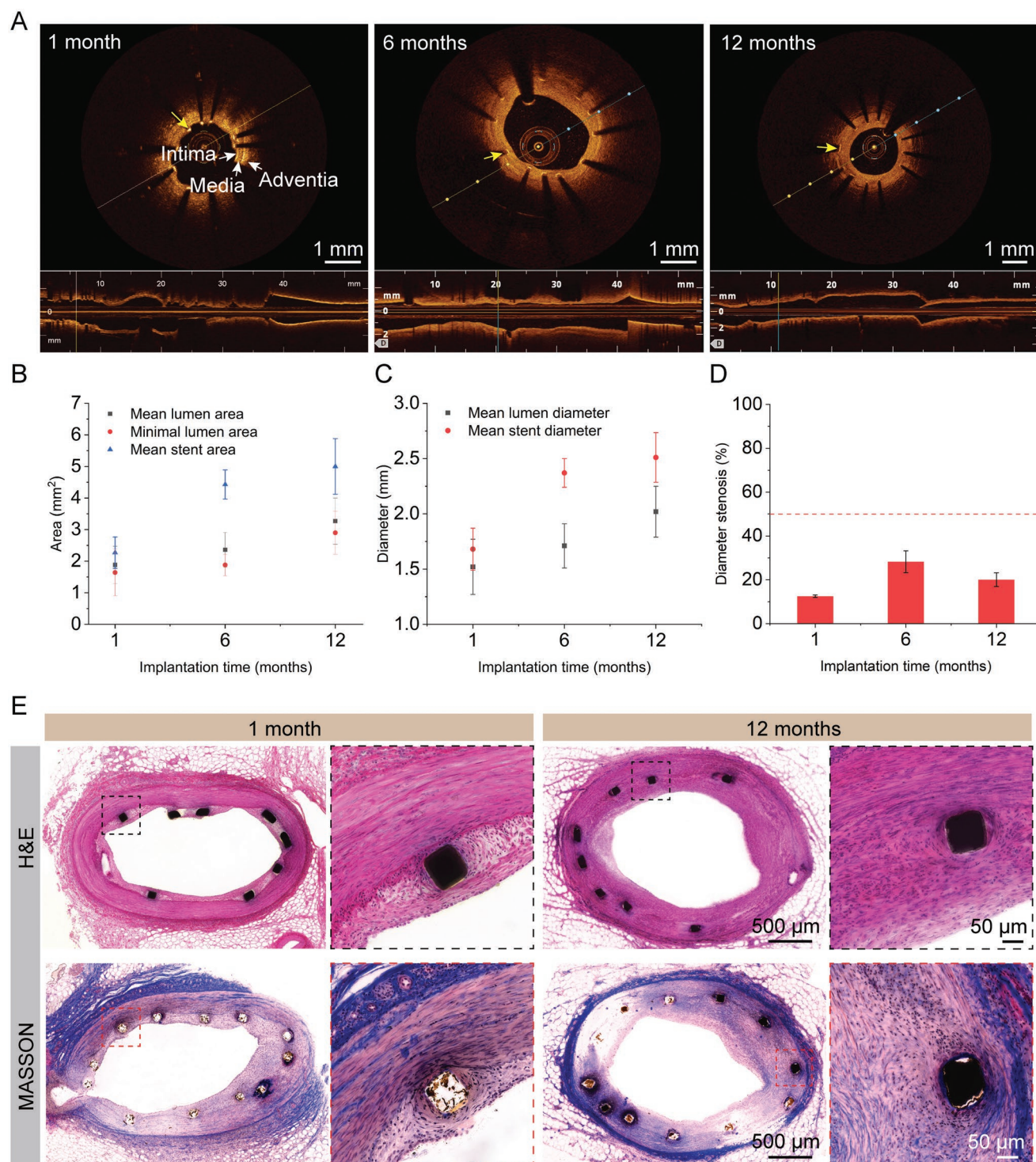


Figure 7. A) Optical coherence tomography (OCT) images of scaffolded segments at 1, 6, and 12 months. The yellow arrows indicate the scaffold strut. B) Lumen area, C) lumen diameter, and D) lumen diameter stenosis (1 month [$n = 6$], 6 months [$n = 9$], 12 months [$n = 12$]). The red dotted line indicates the diagnostic threshold for stenosis. E) Hematoxylin–eosin (H&E) and Masson's trichrome staining of representative sections at 1 and 12 months. Rectangles indicate magnifications.

a rapid endothelialization before 1 month, which is critical to prevent the in-scaffold thrombosis. H&E staining showed mild inflammatory reaction localized around the scaffold struts and

a favorable neointimal recovery process throughout the 1-year implantation. Masson staining illustrated increasing collagen secretion in the neointima with time.

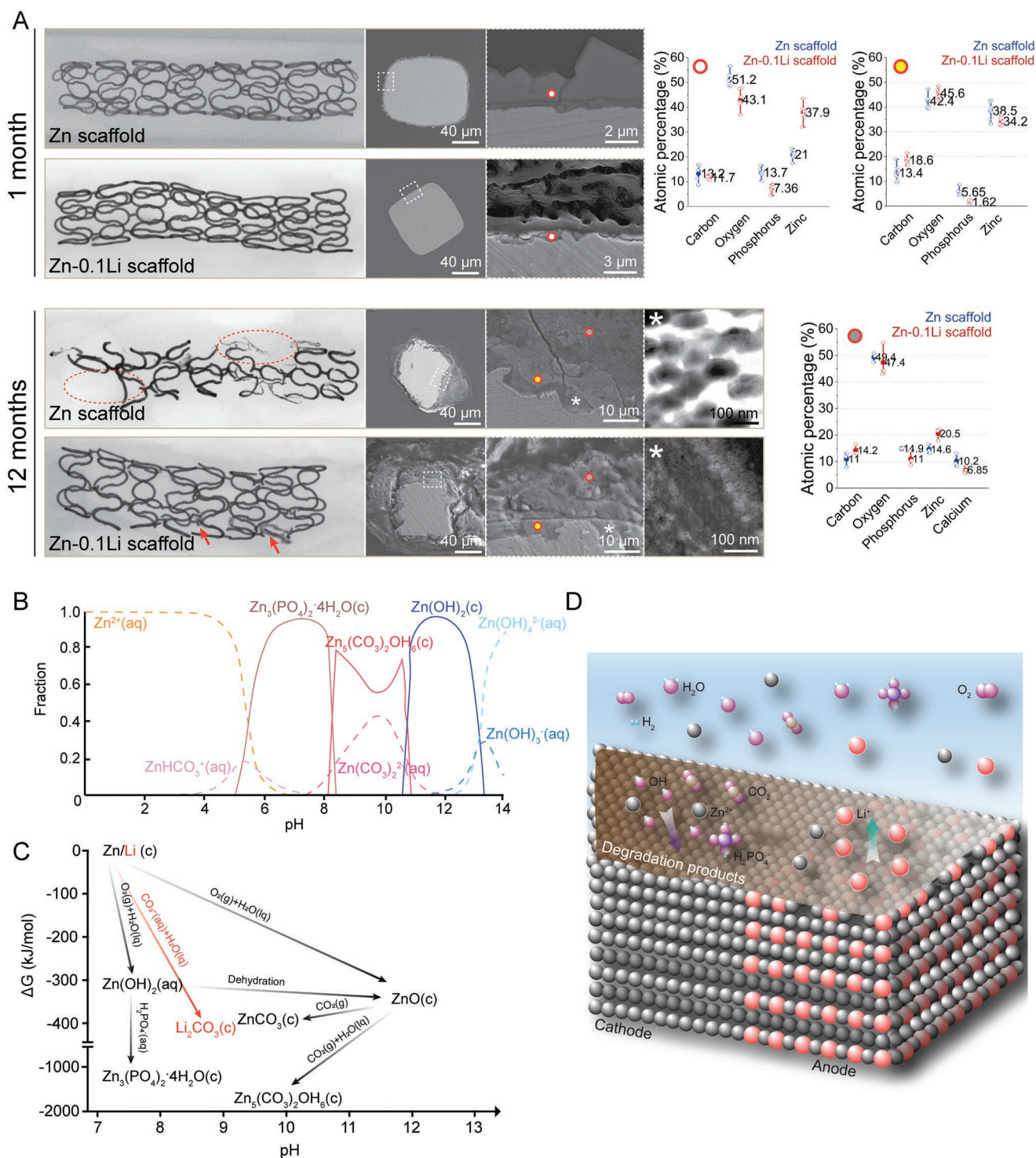


Figure 8. The impact of Li on the biodegradation behavior of Zn scaffold. A) Degradation morphology and composition analysis on in vivo degradation products of the Zn-0.1Li scaffold and pure Zn scaffold at 1 and 12 months. The red circles and arrows indicate absorbed struts and localized degradation, respectively. The white squares and asterisks mark the corresponding magnifications. The white, yellow, and gray dots indicate areas for quantitative elemental analysis. For the box-whiskers plots, the first and third lines correspond to 25th and 75th percentiles, the second line corresponds to median, circles indicate the mean value, and the whiskers include minimum and maximum of all data points. Composition analysis for 1 month ($n = 7$), for 12 months (yellow dot, $n = 7$; gray dot, $n = 3$). B) The fraction of zinc species as a function of pH in simulated body fluid based on the thermodynamic stability constants simulated by Hydra-Medusa. The parameters for simulation are listed in Table S1, Supporting Information. C) Thermodynamic formation pathways of major degradation products during the biodegradation of Zn-0.1Li scaffold according to Figure 8B and Table 3. D) Schematic diagram of the biodegradation mechanism of Zn-0.1Li scaffold.

Table 2. Comparison of the degradation behavior between the pure Zn scaffold and the Zn–0.1Li scaffold.

	Volume loss [12 months]	Penetration rates [$\mu\text{m}/\text{year}$]			Degradation mode		Major degradation products	
		1 M	6 M	12 M	1 M	6–12 M	1 M	12 M
Pure Zn scaffold ^[8]	41.75 \pm 29.72	28.11 \pm 6.47	16.85 \pm 19.39	19.83 \pm 20.38	Uniform	Localized	Zn ₃ (PO ₄) ₂ ·4H ₂ O	ZnO, ZnCO ₃ , Ca ₃ (PO ₄) ₂
Zn–0.1Li scaffold	5.03 \pm 3.77	7.89 \pm 4.06	3.92 \pm 2.86	2.93 \pm 2.12	Uniform	Localized	ZnO, ZnCO ₃ , Li ₂ CO ₃	ZnO, ZnCO ₃ , Li ₂ CO ₃ , Ca ₃ (PO ₄) ₂

3. Discussion

3.1. Optimization Effect of Li on the Mechanical Performance of Zn Scaffold

Vascular stents undergo a severe plastic deformation during crimping and expansion. The stent should be strong enough to support the diseased vessel for a sufficiently long period of time (>3–6 months). Meanwhile, the strut thickness should not be too thick to induce adverse events such as in-stent restenosis and stent thrombosis.^[9a] Therefore, stent materials must have extraordinary mechanical properties to ensure the safety and effectiveness of clinical treatment. The basic mechanical requirements for biodegradable materials are proposed as reasonably low yield strength (200–300 MPa), high ultimate tensile strength (>300 MPa), and adequate ductility (>20–30%).^[11] Pure Zn is not suitable as scaffold materials due to its low strength (<160 MPa). The pure Zn has a low stacking fault energy which results in easily dynamic recrystallization (recrystallization temperature 73–143 °C) during thermal processing.^[18] The tube was drawn at 200 °C under severe plastic deformation. As a result, an inhomogeneous coarse microstructure forms in the pure Zn tube with the grain size distribution ranging from 174.76 to 1.79 μm . This microstructure may easily lead to crack propagation and failure during the scaffold crimping and expansion process. We find out that alloying with 0.1 wt% of Li optimize the overall performance of Zn significantly (yield strength 350 MPa, ultimate tensile strength 430 MPa, ductility 28%), but further addition of Li embrittle the material.^[10] The solubility of Li in Zn is about 0.12 wt% at 403 °C according to the phase diagram. A recent study reported a concentration of 0.01 wt% of Li solved in the Zn matrix at room temperature.^[19] The Zn–0.1Li tube consists of ultrafine Zn matrix and nanoscale LiZn₄ phase. The average grain diameter is 2.28 μm , grains smaller than 2 μm account for more than 65% while 20% of the grains reach the sub-micrometer level (Figure 1B). Grain refinement strengthens the material while promoting the plastic deformability via grain boundary sliding. Its industrial counterpart Zn–Al alloy performs room temperature superplasticity (elongation of 125%) when its grain size reduces to 1.3 μm and sub-micrometer level. Precipitation strengthening may be another mechanism contributing to the improved radial strength of the Zn–Li scaffold. The LiZn₄ phase dissolves into the Zn matrix to form supersaturated solid solution during the homogenization process (350 °C, 48 h, water quenching), followed by the precipitation of nanoparticles during the drawing process. These nanoparticles may serve as the core of heterogeneous nucleation to refine the grain during deformation.

More importantly, homogeneously distributed nanoprecipitates can effectively strengthen the material by impeding dislocation sliding. Previous work has revealed a critical role of high density ($7.16 \times 10^{22} \text{ m}^{-3}$) metastable Li rich nanoprecipitates on strengthening hot-warm rolled Zn–Li alloy.^[19] As a result, a 65 μm ultrathin-strut Zn–0.1Li scaffold is accomplished with twofold the radial strength and only 40% of the strut thickness compared to the pure Zn scaffold.

3.2. Impact of Li on the Biodegradation Mechanism of Zn Scaffold

To have a fundamental understanding of the impact of Li on the biodegradation mechanism of Zn scaffold, we compare the differences in degradation behavior between the pure Zn scaffold and the Zn–0.1Li scaffold in Figure 8 and Table 2. Both scaffolds show a uniform degradation mode on macro- and microlevels at the early stage of implantation (1 month). The metallic scaffold remains intact from a macro perspective. When zooming in to the material–tissue interface, a layer of compact and complete degradation product is found covering the metal matrix. We have explained the critical role of blood flow in shaping this uniform mode of degradation in our previous study.^[8] But the two scaffolds manifest great distinct in terms of the morphology and chemical composition of the degradation product layers. The layer of the Zn–0.1Li scaffold is less than 1 μm compared to the 3–5 μm thickness of the pure Zn scaffold. The ratio of Zn:O reduces from 0.88 of the Zn–0.1Li scaffold to 0.41 of the pure Zn scaffold in addition to a great decrease of P content. These results indicate two important messages: 1) the degradation product layer in the Zn–0.1Li scaffold is more protective than that of the pure Zn scaffold. 2) The major degradation products change from Zn₃(PO₄)₂·4H₂O (hopeite) in the pure Zn scaffold to ZnO in the Zn–0.1Li scaffold. Additionally, we should keep in mind that Li is immeasurable by EDS. Li₂CO₃ is generated in the degradation products of the Zn–0.1Li alloy according to the XPS results (Figure 2C). At the late stage of implantation (12 months), the two scaffolds show distinct degradation features on both macro- and microlevels. Non-uniform degradation mode is predominant for both scaffolds. The pure Zn scaffold loses about 41.75% of its volume, and the degraded scaffold struts are invisible under X-ray image (marked by red dotted circles), implying a complete absorption of the metal and products. In contrast, the Zn–0.1Li scaffold shows a more complete and clear geometry except for some blurry parts caused by degradation (marked

Table 3. Gibbs energies of formation and reactions, and solubility product constants of major products formed during the biodegradation of the Zn-based scaffold in the standard state (298.15 K, 1 atm^[25]) and the simulated body fluid (310.15 K, 1 atm).

Degradation products	$\Delta_f G^\circ$ [kJ mol ⁻¹] [298.15 K]	K_{sp} [298.15 K]	K_{sp} [310.15 K]	Reaction equations	$\Delta_r G^\circ$ [kJ mol ⁻¹] [298.15 K]	$\Delta_r G^\circ$ [kJ mol ⁻¹] [310.15 K]
Zn(OH) ₂ (c)	-553.59	3×10^{-17}	1.84×10^{-17}	$2\text{Zn(c)} + \text{O}_2(\text{g}) + 2\text{H}_2\text{O(l)} = 2\text{Zn(OH)}_2(\text{aq})$	-637.78	-618.8
ZnO(c)	-320.52	2.5×10^{-17}	3.31×10^{-17}	$\text{Zn(OH)}_2(\text{aq}) = \text{ZnO(c)} + \text{H}_2\text{O(l)}$	-29.06	-37.34
ZnCO ₃ (c)	-731.57	1.46×10^{-10}	1.23×10^{-10}	$\text{ZnO(c)} + \text{CO}_2(\text{aq}) = \text{ZnCO}_3(\text{c})$	-47.04	-46.11
Zn ₅ (CO ₃) ₂ OH ₆ (c)	-3164.6	—	—	$5\text{ZnO(c)} + 2\text{CO}_2(\text{aq}) + 3\text{H}_2\text{O(l)} = \text{Zn}_5(\text{CO}_3)_2\text{OH}_6(\text{c})$	-79.99	-71.97
Zn ₃ (PO ₄) ₂ ·4H ₂ O(c)	-3616.4	9×10^{-33}	5.35×10^{-34}	$3\text{Zn(OH)}_2(\text{aq}) + 2\text{H}_2\text{PO}_4^-(\text{aq}) = \text{Zn}_3(\text{PO}_4)_2 \cdot 4\text{H}_2\text{O(c)} + 2\text{OH}^-(\text{aq})$	-110.47	—
LiOH(c)	-439	2.29	—	$2\text{Li(c)} + 2\text{H}_2\text{O(l)} = 2\text{LiOH(c)} + \text{H}_2(\text{g})$	-398.59	-397.77
Li ₂ CO ₃ (c)	-1132.12	2.5×10^{-2}	1.27×10^{-6}	$2\text{LiOH(c)} + \text{CO}_3^{2-}(\text{aq}) = \text{Li}_2\text{CO}_3(\text{c}) + 2\text{OH}^-(\text{aq})$	-31.72	—

by red arrows). At the material–tissue interface, the metallic part of both scaffolds is degrading over time. Nevertheless, degradation products in the pure Zn scaffold exhibit a porous morphology and incomplete feature, showing a “dissolving” trait. As for the Zn–0.1Li scaffold, the degradation products are dense and accumulating around the entire metallic matrix. The chemical composition of degradation products are similar in the two scaffolds without considering the existence of Li. Li enriches in degradation products as shown by TOF-SIMS mapping, and Li₂CO₃ is identified by SAED at 12 months.

To figure out the impact of Li on the formation and evolution of degradation products, their thermodynamic parameters (standard state and physiological conditions) are calculated and listed in Table 3. Figure 8B,C depicts the relation of degradation products with pH, and their proposed thermodynamic formation pathway under physiological conditions. Zn can easily react with body fluid to form Zn(OH)₂ under neutral physiological condition. Further formation of ZnO seeds and nucleation process are facilitated by a slow dehydration reaction at body temperature.^[20] There are several mechanisms reported to describe the phase transformation from Zn(OH)₂ to ZnO including the dissolution–reprecipitation mechanism, in situ crystallization mechanism, and solid–solid phase transformation mechanism.^[21] However, Zn₃(PO₄)₂·4H₂O is thermodynamically more favored than ZnO in neutral body fluid, such as blood, under the existence of phosphate groups. The fraction of hopeite among zinc species is higher than 90% at pH 6–8 based on the thermodynamic calculation. In the pure Zn scaffold, the anode and cathode sites are formed spontaneously under the influence of internal or external factors. This phenomenon is clearly illustrated by SVET as a 44 mV of potential difference is formed in the pure zinc surface within 24 h (Figure 2). In blood fluid, the pure Zn scaffold degrades uniformly under conditions of high mass transfer efficiency, strong buffer capacity, and the formation of compact hopeite (1 month). In neointimal tissue (12 months), localized corrosion is more favored as a result of the slower diffusion environment and weaker buffer capacity. The anode site of Zn creates an acidic local pH (down to 5.84) due to the hydrolysis reaction of Zn²⁺ ions.^[22] This low pH zone further facilitate the dissolution of Zn and its degradation prod-

ucts as shown in the degradation morphology of pure Zn scaffold at 12 months (Figure 8A). The Zn–0.1Li scaffold consists of ultrafine Zn matrix, uniformly distributed LiZn₄ phase and Li-rich nanoprecipitates. This refined microstructure actively reacts with body solution to produce Li₂CO₃. After the near surface zone becomes Li-depleted, the reactions among Zn, H₂O, and dissolved O₂ dominate the degradation and generate ZnO and carbonates like Zn₂(CO₃)₂OH₆ and ZnCO₃. The solubility of Li₂CO₃ is three to five orders of magnitude greater than the degradation products of Zn, and is thermodynamically stable at pH > 9.8.^[23] This sparingly soluble Li₂CO₃ has been reported to have self-healing behavior that reforms rapidly if the surface is damaged.^[24] Hydrolysis of Li₂CO₃ produces OH⁻ maintaining the alkaline of the local microenvironment, which may play a critical role in stabilizing the degradation products (oxide and carbonates) of Zn. Electrochemical impedance spectroscopy (EIS) and SVET measurements show higher corrosion resistance and more uniform corrosion potential distribution in Zn–0.1Li alloy compared to the pure Zn. Li₂CO₃ is the major extra products detected in Zn–0.1Li alloy (Figure 2). As a result, although apparent degradation happens in the Zn–0.1Li scaffold at 12 months, the degradation products are preserved in situ instead of dissolving. Therefore, this role of Li can be beneficial to maintain the early structural integrity of the scaffold and continuously prevent the excessive release of soluble ionic products.

3.3. Beneficial Effects of Co-Releasing Zinc and Lithium for Vessel Healing

The dynamic tissue response is highly regulated by the biodegradation behavior and degradation products of the scaffolds. As one of the major products, ionic zinc exhibits significant biological effects on the major effector cells during vessel healing. Ionic zinc has been found to promote smooth muscle cell apoptosis by activating the caspase apoptotic signaling pathway.^[26] The inflammatory response and associated fibrous encapsulation may be regulated by the morphology of degradation layer and releasing ionic zinc.^[27] Interestingly, the effects of ionic

zinc are cell-dependent as endothelial cells remain less affected. A recent study reported a differential effect of ionic zinc on the energy metabolism and mitochondrial function of smooth muscle cells and endothelial cells.^[28] Here, the pure Zn shows good biocompatibility to HUVECs in terms of adhesion and proliferation, but suppresses the cell migration at ionic zinc concentration $0.81\text{--}3.25\text{ }\mu\text{g mL}^{-1}$. Meanwhile, the pure Zn effectively inhibits the proliferation and migration of HASMCs at ionic zinc concentration $2.01\text{--}8.03\text{ }\mu\text{g mL}^{-1}$. The Zn–0.1Li alloy improves the cell migration of HUVECs significantly compared to the pure Zn. Meanwhile, it enhances the inhibitory effect on the migration of HASMCs significantly. The ionic concentrations in pure Zn and Zn–0.1Li alloy extracts are similar except for $\approx 1\text{ }\mu\text{g mL}^{-1}$ ionic lithium. A dose-dependent manner ($0.2\text{--}20\text{ mM}$) of promoting vascular endothelial growth factor expression in endothelial cells is found in lithium.^[29] Additionally, lithium has been reported to inhibit the proliferation and migration of smooth muscle cells and alleviates balloon injury-induced neointima formation via peroxisome proliferator-activated receptor gamma coactivator 1- α pathway.^[30] The co-release of ionic zinc and lithium may perform synergistic effects in positively modulating the activity and function of endothelial cells and smooth muscle cells. The underlying mechanism is worth further investigation.

The impact of biodegradation on the vessel healing process can be indirectly speculated by the precipitation and dissolution equilibrium of degradation products (Figure S2, Supporting Information). In blood flow, the ionic zinc concentration is $0.12\text{ }\mu\text{g mL}^{-1}$ at pH 7.4 when $\text{Zn}_3(\text{PO}_4)_2 \cdot 4\text{H}_2\text{O}$ is the major products. In the Zn–0.1Li scaffold, local alkaline shifts the degradation products from $\text{Zn}_3(\text{PO}_4)_2 \cdot 4\text{H}_2\text{O}$ to ZnO and ZnCO_3 . The ionic zinc concentration ranges from 0.06 to $5.09\text{ }\mu\text{g mL}^{-1}$ at around pH 8 for ionic zinc. In neointima, ZnO and ZnCO_3 remain as the major products. The existence of Li_2CO_3 further stabilizes the products of Zn by maintaining an alkaline microenvironment. The concentration of ionic zinc up to $6.51\text{ }\mu\text{g mL}^{-1}$ shows no impact in the proliferation of endothelial cells, and limited impact in their migration. The normal endothelialization process (within 1 month) in both rabbit abdominal aorta and porcine coronary aorta further verifies the biosafety of the Zn-based scaffold. More importantly, the effective thresholds for ionic zinc to inhibit the proliferation and migration of smooth muscle cells without toxic effects ranges from 2.01 to $8.03\text{ }\mu\text{g mL}^{-1}$. At pH 7.4, the ionic zinc concentration for ZnO to reach equilibrium between precipitation and dissolution is up to $41.2\text{ }\mu\text{g mL}^{-1}$, which is toxic to the smooth muscle cells and may activate the inflammatory response. But the detrimental effects would be reversed once the pH increases to 8.0. Therefore, Li_2CO_3 may act as “a security lock” for the biosafety of Zn-based scaffolds, and endow it with desirable anti-hyperproliferation function. An appropriate histological response was observed throughout the one-year implantation of the Zn–0.1Li scaffold. No severe inflammatory reaction is observed in tissues adjacent to the scaffold struts, and the neointima covers the thin strut within 1 month. The diameter stenosis of biodegradable scaffolds in the porcine coronary artery is plotted in Figure S2B with the golden standard drug-eluting stent (Xience V) as a comparison. In general, stenosis rates of all the biodegradable scaffolds

within 1 year are much lower than the 50% criteria of restenosis, but higher than the value of Xience V. Zn–0.1Li scaffold displays the lowest stenosis rate among all the biodegradable scaffolds at 1 month followed by a peak at 6 months, and then reduced to 20% at 12 months. Considering the effect of everolimus in reducing neointimal hyperplasia in Xience V and Absorb, biodegradable Zn–0.1Li bare metallic scaffold maintains favorable stenosis rate during the 1-year implantation in the porcine coronary artery. The potential anti-hyperproliferation function of the biodegradable Zn–Li vascular scaffold must be systematically investigated in the future study.

4. Conclusion

We have optimized an ultrathin strut biodegradable Zn-based vascular scaffold using a lithium-induced mechanism. Microalloying with Li (0.1 wt%) combined with severe plastic deformation during tube processing leads to an ultrafine uniform microstructure. This microstructure allows the Zn–Li scaffold to achieve twice the radial force with only 40% of the strut thickness of the pure Zn scaffold. The uniformity of scaffold degradation is improved by the homogeneous distribution of nanoscale Li-containing phases, which degrade preferentially and generate Li_2CO_3 to stabilize the Zn products. Meanwhile, the co-release of ionic zinc and lithium enhances the differential effects on activities of endothelial cells and smooth muscle cells during scaffold degradation. The Zn–Li bare metallic scaffold exhibits a good profile in facilitating the endothelialization process and preventing intimal hyperplasia. These findings provide a systematic exploration and validation of a next-generation biodegradable vascular scaffold with comparable mechanical performance to durable metallic stents and potential biofunctions to advance vessel healing.

5. Experimental Section

Study Design: The main purpose of this study was to investigate the fundamental impact of Li on the mechanical performance, biodegradation behavior, and biological effects of biodegradable Zn-based scaffolds. The microstructure of Zn–0.1Li microtubes was examined by EBSD and transmission electron microscopy (TEM). The corrosion behavior was investigated with the EIS and the SVET system. Impact of materials on cell proliferation and migration were studied by using HUVECs and HASMCs. Zn–0.1Li scaffolds were implanted into the coronary arteries of Barna pigs. Degradation of the Zn–0.1Li scaffold was studied by a multistage analysis. Micro-CT was used to observe the degradation profile of scaffolds at a macrolevel. The microscopic appearance of the scaffold and analysis of corresponding degradation products were performed by SEM, TEM, and TOF-SIMS. Six Barna pigs (mean weight, 30 kg) were purchased from Songlian Experimental Animal Farm (Shanghai, China). Each pig was implanted with two Zn–0.1Li scaffolds. All surgical procedures were conducted according to the ARRIVE guidelines (Animal Research: Reporting of in Vivo Experiments) and approved by the Animal Ethics Committees of Shanghai Children's Medical Center, Shanghai Jiaotong University.

For the Zn–0.1Li alloy and pure Zn samples, corrosion study included the data of EIS ($n = 4$), corrosion potential ($n = 3$), and pH values ($n = 3$). Cell study included the data of proliferation ($n = 9$ for direct contact test, $n = 5$ for indirect contact test) and migration ($n = 5$). For the Zn–0.1Li scaffold, mechanical performance included the data of strut

thickness ($n = 3$), crossing profile ($n = 3$), recoil ($n = 3$), foreshortening ($n = 3$), and radial strength ($n = 3$); Micro-CT results included the data at 1 month ($n = 3$), 6 months ($n = 3$), and 12 months ($n = 4$) post-surgery; penetration rates, cross sectional analysis, and ARDP included the data at 1 month ($n = 24$), 6 months ($n = 25$), and 12 months ($n = 20$) post-surgery; chemical composition of degradation products included the data at 1 month ($n = 7$), 6 months ($n = 16$), and 12 months ($n = 18$) post-surgery; OCT quantitative analysis included the data at 1 month ($n = 3$), 6 months ($n = 3$), and 12 months ($n = 4$) post-surgery.

Scaffold Fabrication and Characterization: The Zn–0.1Li alloy was designed by Peking University and used as the starting material. The as-cast alloy was homogenized at 350 °C for 48 h followed by water quenching. Then, hot extrusion was performed at a ratio of 36:1, 1 mm s^{−1} at 260 °C. The as-extruded Zn–0.1Li alloy was further processed into microtubes (Φ3.0 × 0.1 mm) by Southeast University. These tubes were manufactured into scaffolds (Φ3.0 × 0.065 mm) by laser cutting, chemical etching, and electropolishing. The crossing profile for the scaffold system was defined as the maximum diameter found in the scaffold crimped segment and measured using a digital microscope (VHX-700F, KEYENCE, Japan). Foreshortening was calculated from Equation (1):^[7b]

$$\text{Foreshortening (\%)} = 100 \times \left[1 - \left(\frac{\text{Length}_{\text{inflated}}}{\text{Length}_{\text{original}}} \right) \right] \quad (1)$$

where Length_{inflated} was the length of the scaffold after inflation and Length_{original} was the original length of the scaffold before inflation.

Recoil was calculated from Equation (2):^[7b]

$$\text{Recoil (\%)} = 100 \times \left[1 - \left(\frac{\text{Diameter}_{\text{final}}}{\text{Diameter}_{\text{inflated}}} \right) \right] \quad (2)$$

where Diameter_{final} was the outer diameter of the scaffold after deflation of the delivery balloon and Diameter_{inflated} was the outer diameter of the scaffold while the delivery balloon was inflated. Radial curves were measured at a compression rate of 0.1 mm s^{−1} using a radial strength tester (RX550-100, Machine Solution Inc., USA). The radial strength (kPa) was defined as the strength at 10% compression deformation.

Microstructure Characterization of Microtubes: The microtubes of pure Zn and Zn–0.1Li alloy were embedded in resin. The cross section that was perpendicular to the drawing direction of tubes was polished by Ar⁺ ion at 1 keV for 30 min in an ion thinning machine (Leica EM RES102). Grain boundary maps and inverse pole figures were detected by EBSD (EDAX Velocity Super) in a SEM (JSM 7200F). Sample for TEM was thinned to about 60 nm thick by FIB. Bright-field images, high-resolution images, and SAED patterns were pictured by an FEI TEM (FEI Talos F200X). XRD (Bruker D8 Advance) using CuKα was operated at 40 kV and 40 mA to identify the phase composition of samples at a scan rate of 2° min^{−1} with step of 0.02°.

Corrosion Tests: The EIS measurement was carried out using a three-electrode system (work electrode, count electrode [Pt], and saturated calomel electrode) in an electrochemical working station (Autolab, Metrohm, Switzerland) at 37 °C in SBF (HANKS' balanced salt mixture, Solarbio, Beijing). Samples were immersed for 1, 12, and 24 h before data collecting. The open-circuit potential (OCP) was monitored for 3600 s. EIS was conducted by applying 10 mV perturbation to OCP value in a frequency range from 10⁵ to 10^{−2} Hz. Five samples in each group were measured for parallel. The SVET system (Applicable Electronics Inc., USA) was used to detect the dynamic corrosion potential and pH values of sample surface in SBF for 1, 12, and 24 h. After immersion, samples were rinsed by deionized water and blow dry. The corrosion morphology was pictured by an SEM (Hitachi S-4800, Japan). An XPS (NAP-XPS, Specs, Germany) was utilized to analyze the chemical composition of corrosion products. The C 1s peak was calibrated by using the hydrocarbon contamination C 1s peak at 284.5 eV.

Cell Study: HUVECs (ATCC CRL-1730) and HASMCs (CTCC-900-0268) were used here to evaluate the impact of materials on cell adhesion, proliferation, and migration. HUVECs were cultured with Dulbecco's

modified Eagle's medium with 10% fetal bovine serum (FBS), 100 U mL^{−1} penicillin, and 100 μg mL^{−1} streptomycin at 37 °C in a humidified atmosphere of 5% CO₂. HASMCs were cultured with a special complete cell medium (CTCC-900-0268-M, Meisen). Each side of sample was disinfected by UV light for at least 1 h. Extracts were prepared by immersing samples (Φ10 × 1 mm) into the complete cell culture medium at a ratio of 1.25 mL cm^{−2} under the same cell culture conditions for 24 h. The supernatant fluid was withdrawn, centrifuged, and diluted prior to use.

For adhesion, 50 μL of cell suspension at a density of 2 × 10⁵ cell mL^{−1} was seeded on the sample surface for 1 h followed by using phosphate buffered saline (PBS) to wash non-adherent cells for three times. Then, cells were culture with normal medium for 2 and 6 h before fixed for observation. For SEM (Hitachi S-4800, Japan) observation, samples were rinsed with PBS, and fixed in 2.5% glutaraldehyde solution for 2 h followed by gradient dehydration (100%, 95%, 90%, 80%, 70%, 60%, and 50% ethanol), and air drying. Gold spraying was utilized to improve the conductivity of samples. For confocal (CLSM, Leica TCS SP5, Germany) visualization, 1 mg mL^{−1} DAPI and 1.0% v/v FITC-phalloidin (sigma) were used to stain the nuclei and actin, respectively.

Cell proliferation was studied by direct and indirect test methods. For direct test, cells were seeded on sample surface at a density of 6 × 10⁵ cell mL^{−1} followed by 24, 48, and 72 h culture at 37 °C in a humidified atmosphere of 5% CO₂. For fluorescence microscopy (Olympus, Japan) observation, cells were stained following a Live/Dead staining procedure (Viability/Cytotoxicity Assay Kit for Animal Live & Dead Cells (Calcein, AM EthD-1)). Cell density was performed by counting cell number in random selected areas (three areas for each sample, three samples for each group) using ImageJ pro software. For indirect test, 100 μL of cell suspension was seeded into a 96-well plate at a density of 5 × 10⁴ cell mL^{−1} for each well for 24 h to allow attachment. Then, culture medium was replaced by materials extracts (zero- to three-fold dilution) with culture medium and 10% dimethyl sulfoxide as negative and positive control groups, respectively. After 1, 2, and 4 days' incubation, a cell viability kit (CCK-8, Dojindo, Kumamoto, Japan) was used to measure the cell viability and proliferation. An average of five measurements was taken for each group.

To measure the cell migration, cells were seeded in a 12-well plate and cultured with normal medium for 48–72 h to reach confluency. Then, scratches were created by a 200 μL pipette tip. Damaged cells were washed up with a PBS solution for three times. Material extracts containing 3% FBS were added into each well for 24 h before Live/Dead staining. Cell covered area was calculated using ImageJ pro software. An average of three measurements was taken for each group.

Surgical Procedure: A total of 12 Zn–0.1Li scaffolds were deployed in the right coronary artery and the left anterior descending coronary artery of six Barna pigs. The implantation procedure of pure Zn scaffolds was reported in our previous study.^[9] Each pig was implanted with two scaffolds. All surgical procedures were conducted according to the ARRIVE guidelines (Animal Research: Reporting of In Vivo Experiments) and approved by the Animal Ethics Committees of Shanghai Children's Medical Center, Shanghai Jiaotong University (approval number: 180606). Experiments strictly followed the Guide for the Care and Use of Laboratory Animals (NIH Publications No. 8023, revised 1978). Briefly, intramuscular injection of Zoletil was performed to induce anesthesia, followed by 2% isoflurane to maintain anesthesia during the surgery through orotracheal intubation. Electrocardiogram, arterial oxygen saturation, blood pressure, and heart rate were monitored throughout the operation. Experimental animals were placed in the supine position with the right thigh sterilized. The femoral artery was punctured at the pulsation point. A 7F catheter sheath was introduced with a short straight guide wire when the whole body was heparinized (0.2 mg/100 g). A 7F single-curved catheter was inserted into the sheath for angiography. After confirming the coronary artery, a balloon catheter was inserted through the sheath to deploy the scaffold in the middle of coronary artery. Finally, the catheter was withdrawn and the puncture point was pressed for 3 min until bleeding stopped. Antibiotics were given intramuscular for 7 days after the operation to prevent infection.

Long-term oral aspirin antiplatelet therapy was used after surgery. At 1-, 6-, and 12-month post-surgery, OCT was conducted to evaluate stenosis, neointimal hyperplasia, and thrombosis in scaffolded arteries. Diameter stenosis was calculated from Equation (3):

$$\text{Diameter stenosis (\%)} = 100 \times \frac{(\text{Scaffold diameter} - \text{Lumen diameter})}{\text{Scaffold diameter}} \quad (3)$$

Micro-CT Characterization: Explanted arteries with Zn–0.1Li scaffolds were characterized by a Skyscan 1172 Micro-CT system (Bruker Micro-CT N.V., Kontich, Belgium). A 9 μm resolution protocol (59 kV, 155 μA , Al 0.5 filter, rotation step 0.2°, frame averaging 2°) was used for scanning. CT images were reconstructed by using Skyscan NRecon software and analyzed via CTAn, CTVol software to generate volume loss data (Bruker Micro-CT N.V., Kontich, Belgium).

Cross-Sectional Analysis: Scaffolded arteries were embedded in methyl methacrylate and the subsequent blocks were slice to create sections of 1 mm thickness. Three arteries were used with a least three sections selected from proximal, middle, and distal of each artery at each time point (1, 6, and 12 months). Sections were prepared by grinding with 7000 grit SiC paper, polishing with 0.1 μm diamond paste, and coating with a thin layer of gold before visualization. Sections were examined under a SEM (Hitachi S-4800, Japan) equipped with an EDAX EDS system. Elemental mappings and selected area analysis were conducted in regions of interest. Obtained images were further analyzed by using Image-Pro Plus 6.0 to generate penetration rate, CSA reduction, and ARDP based on a protocol reported by Bowen et al.^[7a]

Transmission Electron Microscopy Analysis: Thin discs cut from these Cu-containing materials were mechanically ground and polished. Subsequently, from these finely polished discs, TEM specimens were prepared by in situ lift-out technique in a dual-beam system (Tescan GAIA3) and further thinned to about 100 nm thick by FIB of Ga⁺ at 5 kV, 15 pA. The TEM study was carried out in a JEM 2100F equipped with Bruker EDS and Gatan EELS/GIF systems operating at 200 keV.

FIB-SEM/TOF-SIMS Procedure: The Ga⁺ source-based FIB-SEM (GAIA3, Tescan, Czech Republic) and TOF-SIMS (ToFwerk AG, Switzerland) system were used for chemical mapping. The acquisition was carried out at the ion beam energy and current of 30 keV and 500 pA. Maps consisting of 512 \times 512 pixels covering the same field of view of 10 \times 10 μm^2 were collected with the pixel resolution of 19.5 nm in both x- and y-directions. The material was sputtered away, frame by frame, and secondary ions were generated from an increasing depth in the specimen. The secondary ions were extracted and passed through the TOF-SIMS analyzer, producing mass spectra for each point in the map. In order to compile 2D maps, the total spectra for each specific location within the 2D map (pixel) were integrated sequentially of 100 frames, corresponding to the overall depth of about 1.0 μm .

Histological Analysis: Scaffolded arteries were processed and embedded in methyl methacrylate. Three arteries were used with a least three sections selected from proximal, middle, and distal of each artery at each time point (1, 6, and 12 months). Each slice was cut and grinded into 5 μm thickness for H&E and Masson's trichrome (collagen) staining. Samples were visualized under a high-quality microscope (Olympus CKX41, Japan).

Thermodynamic Analysis: An inductively coupled plasma optical emission spectroscope (iCAP6300, Thermo) was used to measure ionic Zn concentrations of ZnO, Zn(OH)₂, ZnCO₃, Zn₂(CO₃)₂·OH₂, and Zn₃(PO₄)₂·4H₂O during precipitation-dissolution equilibrium at pH 6, 7.4, and 8 in a SBF solution at 37 °C. Then, Medusa software (designed by KTH Royal Institute of Technology, Sweden) was used to create the relations between degradation product fractions and pH using the calculated hydrolysis equilibrium constants.

Statistical Analysis: The data were evaluated by one-way analysis of variance followed by post hoc Tukey's multiple comparison test using Origin 2019b software. The data were presented as mean \pm standard deviation ($n \geq 3$, independent samples), and the significance of a difference was analyzed at levels of * $p < 0.05$, ** $p < 0.01$, and *** $p < 0.005$.

Supporting Information

Supporting Information is available from the Wiley Online Library or from the author.

Acknowledgements

H.Y. and D.J. contributed equally to this work. This work is supported by the Natural Science Foundation of China (Grant Nos. U22A20121, 51931001, 5193000081, 5210010632, and 52171237), the Fundamental Research Funds for the Central Universities (Grant Nos. JKF-YG-21-B003, YWF-22-T-105, and YWF-22-L-1264), and the Non-profit Central Research Institute Fund of National Research for Family Planning (Grant No. 2022GJM03). Dr. Y. Z. Wang in Shanghai Equshine Scientific Instruments Co., Ltd. offered great help in analyzing the results of SVET data.

Conflict of Interest

The authors declare no conflict of interest.

Data Availability Statement

The data that support the findings of this study are available from the corresponding author upon reasonable request.

Keywords

biodegradation mechanisms, biological effects, mechanical performance, ultrathin-strut scaffolds, Zn–Li alloys

Received: February 3, 2023

Revised: February 27, 2023

Published online: March 28, 2023

- [1] a) T. Pilgrim, R. Piccolo, D. Heg, M. Roffi, D. Tüller, O. Muller, I. Moarof, G. C. Siontis, S. Cook, D. Weilenmann, *Lancet* **2018**, 392, 737; b) S. Bangalore, B. Toklu, N. Patel, F. Feit, G. W. Stone, *Circulation* **2018**, 138, 2216.
- [2] a) I. Javadi, O. Yoshinobu, O. John, A. Alexandre, W. Ron, S. Patrick, *Eur. Heart J.* **2014**, 35, 765; b) J. Ormiston, M. J. Webster, *Lancet* **2007**, 369, 1839.
- [3] C. Indolfi, S. De Rosa, A. Colombo, *Nat. Rev. Cardiol.* **2016**, 13, 719.
- [4] a) H. Jinnouchi, S. Torii, A. Sakamoto, F. D. Kolodgie, R. Virmani, A. V. Finn, *Nat. Rev. Cardiol.* **2019**, 16, 286; b) P. W. Serruys, J. A. Ormiston, Y. Onuma, E. Regar, N. Gonzalo, H. M. Garcia-Garcia, K. Nieman, N. Bruining, C. Dorange, K. Miquel-Hébert, *Lancet* **2009**, 373, 897.
- [5] a) M. Zewski, M. J. Kubisa, C. Eyleten, S. D. Rosa, M. Postua, *J. Clin. Med.* **2019**, 8, 145; b) G. Caiazzo, I. D. Kilic, E. Fabris, R. Serdoz, A. Mattesini, N. Foin, S. De Rosa, C. Indolfi, C. Di Mario, *Int. J. Cardiol.* **2015**, 201, 129.
- [6] a) J. Bennett, Q. De Hemptinne, K. McCutcheon, *Expert Rev. Med. Devices* **2019**, 16, 757; b) M. Haude, R. Erbel, P. Erne, S. Verheye, H. Degen, D. Böse, P. Vermeersch, I. Wijnbergen, N. Weissman, F. Prati, *Lancet* **2013**, 381, 836; c) M. Haude, H. Ince, A. Abizaid, R. Toelg, P. A. Lemos, C. von Birgelen, E. H. Christiansen, W. Wijns, F. J. Neumann, C. Kaiser, *Lancet* **2016**, 387, 31.

- [7] a) P. K. Bowen, J. Drelich, J. Goldman, *Adv. Mater.* **2013**, 25, 2577; b) P. K. Bowen, R. J. Guillory, E. R. Shearier, J. M. Seitz, J. Drelich, M. Bocks, F. Zhao, J. Goldman, *Mater. Sci. Eng., C* **2015**, 56, 467.
- [8] H. Yang, C. Wang, C. Liu, H. Chen, Y. Wu, J. Han, Z. Jia, W. Lin, D. Zhang, W. Li, *Biomaterials* **2017**, 145, 92.
- [9] a) A. Kastrati, J. Mehili, J. Dirschinger, F. Dotzer, H. Schühlen, F.-J. Neumann, M. Fleckenstein, C. Pfaffert, M. Seyfarth, A. Schömig, *Circulation* **2001**, 103, 2816; b) N. Foin, R. D. Lee, R. Torii, J. L. Guitierrez-Chico, A. Mattesini, S. Nijjer, S. Sen, R. Petraco, J. E. Davies, C. J. Di Mario, *Int. J. Cardiol.* **2014**, 177, 800.
- [10] H. Yang, B. Jia, Z. Zhang, X. Qu, G. Li, W. Lin, D. Zhu, K. Dai, Y. Zheng, *Nat. Commun.* **2020**, 11, 401.
- [11] E. Mostaed, M. Sikora-Jasinska, J. W. Drelich, M. Vedani, *Acta Biomater.* **2018**, 71, 1.
- [12] C. M. Agrawal, K. F. Haas, D. Leopold, H. G. Clark, *Biomaterials* **1992**, 13, 176.
- [13] C. Zhou, H. F. Li, Y. X. Yin, Z. Z. Shi, H. J. Zhang, *Acta Biomater.* **2019**, 97, 657.
- [14] W. Lin, L. Qin, H. Qi, D. Zhang, G. Zhang, R. Gao, H. Qiu, Y. Xia, P. Cao, X. Wang, *Acta Biomater.* **2017**, 54, 454.
- [15] W. Schmidt, P. Behrens, C. B. Wunderlich, S. Siewert, N. Grabow, *Cardiovasc. Revasc. Med.* **2016**, 17, 375.
- [16] J. P. Oberhauser, S. Hossainy, R. J. Rapoza, *Eurointervention* **2009**, 5, F15.
- [17] N. Hornsveid, B. Put, W. M. M. Kessels, P. M. Vereeckenbc, M. Creatorea, *RCS Adv.* **2017**, 7, 41359.
- [18] M. E. Kassner, S. R. Barrabes, *Mater. Sci. Eng., A* **2005**, 410, 152.
- [19] Z. Li, Z. Shi, Y. Hao, H. Li, X. Liu, *J. Mater. Sci. Technol.* **2019**, 35, 2618.
- [20] A. Goux, T. Pauporté, J. Chivot, D. Lincot, *Electrochim. Acta* **2005**, 50, 2239.
- [21] M. Wang, Y. Zhou, Y. Zhang, S. H. Hahn, E. J. Kim, *CrystEngComm* **2011**, 13, 6024.
- [22] C. Wang, X. Liu, D. Mei, M. Deng, Y. Zheng, M. L. Zheludkevich, S. V. Lamaka, *Corros. Sci.* **2022**, 197, 110061.
- [23] P. K. Choubey, K. S. Chung, M. S. Kim, J. C. Lee, R. R. Srivastava, *Miner. Eng.* **2017**, 110, 104.
- [24] W. Xu, N. Biribilis, G. Sha, Y. Wang, J. E. Daniels, Y. Xiao, M. Ferry, *Nat. Mater.* **2015**, 14, 1229.
- [25] J. G. Speight, *Lange's Handbook of Chemistry*, McGraw-Hill Education, New York **2017**.
- [26] R. J. Guillory, T. M. Kolesar, A. A. Oliver, J. A. Stuart, J. Goldman, *Mater. Sci. Eng., C* **2020**, 111, 110826.
- [27] R. J. Guillory, P. K. Bowen, S. P. Hopkins, E. R. Shearier, E. J. Earley, A. A. Gillette, E. Aghion, M. Bocks, J. W. Drelich, J. Goldman, *ACS Biomater. Sci. Eng.* **2016**, 2, 2355.
- [28] O. R. Bagshaw, F. Moradi, C. S. Moffatt, H. A. Hettwer, P. Liang, J. Goldman, J. W. Drelich, J. A. Stuart, *Biomater. Biosyst.* **2021**, 4, 100027.
- [29] S. Guo, K. Arai, M. F. Stins, D. M. Chuang, E. H. Lo, *Stroke* **2009**, 40, 652.
- [30] Z. Wang, X. Zhang, S. Chen, D. Wang, J. Wu, T. Liang, C. Liu, *PLoS One* **2013**, 8, e55471.